

Dai, Gaoliang; Degenhardt, Johannes; Hu, Xiukun; Wolff, Helmut; Tutsch, Rainer; Manske, Eberhard

A feasibility study towards traceable calibration of size and form of microspheres by stitching AFM images using ICP point-to-plane algorithm

Original published in: Measurement science and technology. - Bristol : IOP Publ.. - 34 (2023), 5, art. 55009, 13 pp.
Original published: 2023-02-09
ISSN: 1361-6501
DOI: [10.1088/1361-6501/acb6e1](https://doi.org/10.1088/1361-6501/acb6e1)
[Visited: 2023-07-18]



This work is licensed under a [Creative Commons Attribution 4.0 International license](https://creativecommons.org/licenses/by/4.0/). To view a copy of this license, visit <https://creativecommons.org/licenses/by/4.0/>

A feasibility study towards traceable calibration of size and form of microspheres by stitching AFM images using ICP point-to-plane algorithm

Gaoliang Dai^{1,*} , Johannes Degenhardt¹ , Xiukun Hu² , Helmut Wolff¹, Rainer Tutsch³ and Eberhard Manske⁴ 

¹ Physikalisch-Technische Bundesanstalt, Bundesallee 100, Braunschweig 38116, Germany

² College of Materials and Chemistry, China Jiliang University, 310018 Hangzhou, People's Republic of China

³ Technische Universität Braunschweig, IPROM, Schleinitzstraße 20, Braunschweig 38106, Germany

⁴ Institute of Process Measurement and Sensor Technology, Technische Universität Ilmenau, Ilmenau 98694, Germany

E-mail: Gaoliang.Dai@ptb.de

Received 14 October 2022, revised 11 January 2023

Accepted for publication 29 January 2023

Published 9 February 2023



CrossMark

Abstract

We present a new method for traceable calibration of size and form error of microspheres, which was realised by stitching a series of atomic force microscopic (AFM) images measured at different orientations of microspheres using the metrological large range AFM of the PTB. The stitching algorithm is achieved using an iterative closest point point-to-plane algorithm. As the AFM tip geometry is one of the most significant error sources for the developed method, it was traceably calibrated to a line width standard (type IVPS100-PTB), whose feature geometry was calibrated with a traceable route to the lattice constant of crystal silicon. Measurement setup, scan strategy, and data evaluation processes have been detailed in the paper. Measurement results show high stability and robustness of the developed method. For instance, the standard deviation of four repeated measurements reaches 5 nm, indicating promising performance.

Keywords: microsphere, calibration, micro coordinate measuring machine, atomic force microscopy, iterative closest point algorithm, data fusion

(Some figures may appear in colour only in the online journal)

1. Introduction

The sphere is a fundamental geometric object in dimensional metrology. It is the most commonly used form of probing

elements in tactile measurement tools, such as coordinate measuring machines (CMMs) [1] and stylus profilometer [2]. It is widely applied in transfer standards for the physical embodiment of unit or dimension in metrology, such as the silicon spheres applied for the new realization of the SI unit kilogram [3], and the ball-bars, ball-plates and/or ball-trees for the calibration of CMMs [4]. For bigger spheres, techniques for size and form metrology have been well developed and low measurement uncertainty has been achieved. As an example, the measurement of highly enriched ²⁸Si Avogadro spheres with a diameter d of approximately 93 mm can be

* Author to whom any correspondence should be addressed.



Original content from this work may be used under the terms of the [Creative Commons Attribution 4.0 licence](https://creativecommons.org/licenses/by/4.0/). Any further distribution of this work must maintain attribution to the author(s) and the title of the work, journal citation and DOI.

achieved with a measurement uncertainty down to 0.9 nm using a special Fizeau interferometer [5].

The metrology of size and form error of small size spheres, particularly microspheres, remains as a challenge. Small probing spheres are needed in tactile measurement tools to enhance the lateral resolution. Today, ruby spheres with d down to approximately 120 μm and melted fibre probing spheres with d down to 25 μm are applied in micro CMMs [6]. However, due to the limitation of the manufacturing techniques the form error of such small spheres does not scale down with their size; for microspheres with $d < 120 \mu\text{m}$ their form error could even be larger than for bigger spheres [7], becoming a significant or even the most dominant error source in micro CMMs.

Today, several methods have been developed for accurate measurement of microspheres. Tactile methods using micro CMMs [5, 8] are a frequently used technique. A big challenge using this technique is, however, the propagation of size and form error of the probing sphere of the micro CMM to the measurands. To meet this challenge, K ung A and Meli F at the Swiss Federal Office of Metrology (METAS) had developed a method which separates the form error of the sample and probing sphere, thus offering an ultrahigh measurement accuracy without the need of an external reference [9]. In 2011, PTB and METAS had carried out a bilateral comparison on a ruby sphere (nominal d of 1 mm) measured by the micro CMM of METAS [10] and a micro CMM type ‘Zeiss F25’ at the PTB. The discrepancy of their measurement results was approximately 50 nm, which was still significant compared to their evaluated expanded measurement uncertainties ($U = 35 \text{ nm}$ for METAS results and $U = 45 \text{ nm}$ for PTB results, both with the coverage factor of $k = 2$). Recently, Kondo *et al* [11] reported a highly accurate two-point diameter calibration method of spheres with an expanded uncertainty of 21 nm ($k = 2$) using a micro CMM, whose probe radius was determined with an expanded uncertainty of 10 nm ($k = 2$) using a reference gauge block.

Optical methods have also been used for the measurements of microspheres [12–15]. Michihata *et al* [12] proposed a new method based on the whispering gallery modes (WGMs) of the sphere, which is a kind of non-imaging technique. In its measurement, different WGMs were excited in the sphere using different incident wavelengths, resulting in a wavelength spectral fingerprint that is related to the sphere diameter [12]. More optical methods for measurements of microspheres are, however, based on imaging techniques such as white light interferometry [13] and confocal microscopy [14]. Medicus and Jansen [13] measured the diameter of small spheres (nominal d of 500 μm) using a vision CMM that is also a scanning white light interferometer and achieved an expanded measurement uncertainty ($k = 2$) of 0.17 μm . Schaude *et al* [14] have reported a bidirectional confocal measurement of a microsphere which was placed above a mirror. Thus, he was able to measure the upper hemisphere on the real sphere and the lower hemisphere on the mirrored sphere. The method offers benefits with increased measured pixels from both hemispheres for reducing the measurement uncertainty of determined sphere

radius compared to measurement strategies that only sample from one hemisphere, however, it suffers from the shadowing of the object in measurements.

Atomic force microscopes (AFMs) have also been employed for measurements of microspheres [16–18]. Due to the limit of the tip height and scanning range, measured AFM profiles need to be stitched for the measurements of microspheres, where the stitching accuracy is an important issue. For instance, Oertel and Manske [16, 17] developed a method where they measured ten overlapping profiles using an AFM along one great circle (equator) of a ruby microsphere (nominal d of 150 μm) with each profile covering a spherical angle of 40° . By fine aligning the profiles with each other based on their overlapping parts, the profiles are stitched. To account for the error contribution of the AFM tip geometry, they have characterized the (fitted) radius of the tip apex using a commercial tip characterizer (TGG1 from NT-MDT). By least square fitting the finally obtained circular profile along the equator, they obtained the equator radius of the sphere and roundness error. They achieved a standard deviation of 3.7 nm over six repeated measurements, indicating great potential of the method.

This paper further extends the AFM stitching method for traceable measurements of microspheres concerning mainly three aspects. Firstly, a more accurate calibration method was applied for the characterisation of AFM tip geometry with a traceability approach to the SI unit Metre via the crystal silicon lattice constant. Secondly, the method was extended from the calibration of an equator circle to the calibration of a sphere. Thirdly, an iterative closest point (ICP) point-to-plane algorithm has been utilised for stitching AFM images. Particularly, this study offers a new solution for accurately and traceably calibrating not only the size but also the form deviation of microspheres. It should be stressed that the calibration of form deviation of microspheres is a big metrology challenge remaining today, e.g. for applications such as measurements of free-form or aspherical optics using micro CMMs.

The paper is organised in three main sections. Section 2 introduces the experimental setup, scan strategy and tip correction method. Section 3 details the alignment and merging of the AFM images. Section 4 presents measurement results obtained on a ruby sphere with a nominal radius r of 200 μm in this study.

2. Method

2.1. Measurement setup

The measurement setup was based on the metrological large range AFM (Met. LR-AFM), which was developed at the PTB [19] based on a nanomeasuring machine (NMM) [20]. For rotating the sample along two axes a compact mechanical setup was built, as shown in figure 1(a). A ruby microsphere (Saphirwerk AG) with a nominal radius of 200 μm was glued on a tungsten rod, which was in turn fixed on a motorised rotation stage R1 (SR-2013, SmarAct). The stage R1 was

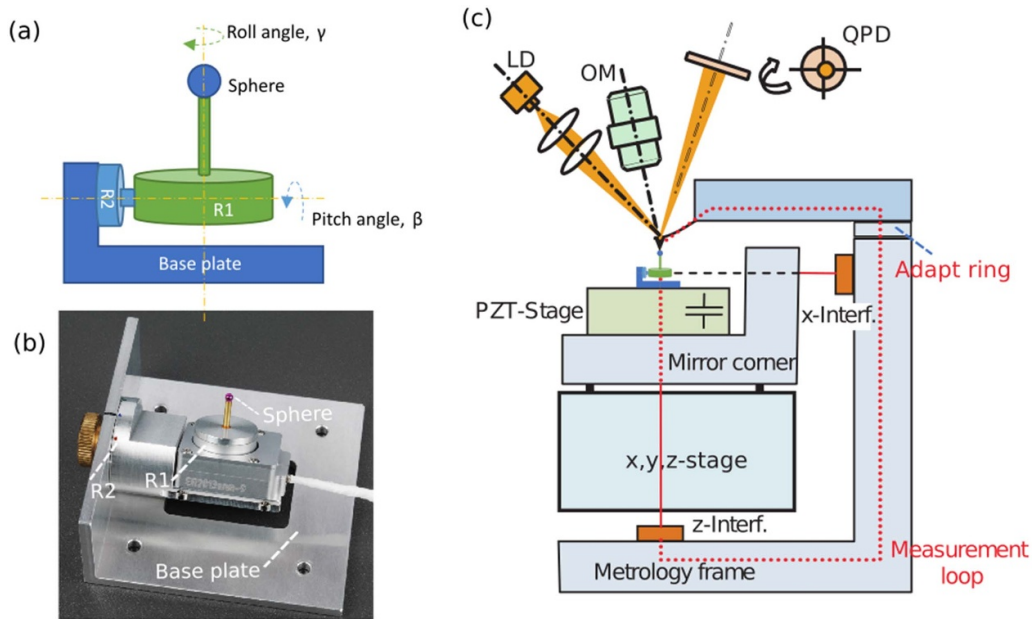


Figure 1. (a) Schematic drawing of the mechanics for rotating and tilting the sphere; (b) photo of the mechanical set up; (c) schematic drawing of the Met. LR-AFM.

fixed to a manual rotation stage R2. Using this mechanical setup, the microsphere can be rotated with a rolling angle γ by R1 and a tilting angle β by R2. In such a way, its spheric surface can be accessed and measured by an AFM tip from the top. A photo of the mechanical setup, which has a size of $60 \text{ mm} \times 60 \text{ mm} \times 25 \text{ mm}$, is shown in figure 1(b).

As the measurement principle of the Met. LR-AFM and its improvements have been published in detail elsewhere [19–22], it is introduced here only briefly. As shown in figure 1(c), the sphere rotation setup (i.e. figure 1(a)) was fixed on a piezo stage (PZT-stage), which was in turn fixed on a mirror corner—the motion platform of the NMM. The mirror corner (together with all mechanics fixed on it and the sphere) was moved by a group of micro stages (x , y , z -stage) along x -, y - and z -axes with a motion range of 25 mm, 25 mm and 5 mm, respectively. The six-degrees-of-freedom of the mirror corner were measured by three interferometers (only that of x - and z -axes are shown in figure 1(c)) and two autocollimators (not shown in figure 1(c)) embedded in the NMM.

The Met. LR-AFM measured in the so-called scanning sample principle. During AFM measurements, the sphere was moved in the xy -plane at the given scan speed solely by the NMM, whereas it was moved by two stages (i.e. the PZT-stage and NMM) using a cascade servo controller along the z -axis. This cascade servo controller simultaneously ran a fast servo loop and a slow servo loop. The fast servo loop quickly moved the sample up- or downward by the PZT-stage to keep the AFM tip–sample interaction constant, whereas the slow servo loop moved the PZT-stage (together with the sample) up- or downward by the z -motion of the NMM so that the motion of the PZT-stage was controlled toward its predefined home position. With this design concept, the Met. LR-AFM has the advantages of a large measurement range and high measurement

speed (please refer to [19] for more details). The nanostructure geometry can be derived from the x -, y -, and z -motions of the two stages. For instance, the z -coordinate of the AFM pixels was calculated from the outputs of the AFM signal, the output of the capacitive sensor embedded in the piezo stage for measuring its z -motion and the value of the z -Interferometer of the NMM, which were simultaneously acquired [22]. Before the measurements, the capacitive sensor and AFM signal were traceably calibrated to the interferometers of the NMM [19]. One frequency stabilized He–Ne laser was used as the light source for all interferometers. Its optical frequency was calibrated at $632\,991\,234 \pm 5 \text{ fm}$ by the optical frequency standard available at the PTB, ensuring direct traceability for the measurements. In recent research, we had improved the correction of high-order nonlinearity error of the z -interferometer, which further improved its metrology performance [23]. A professional software with various measurement strategies [21] was also realised in the Met. LR-AFM, making it a multifunctional and unique workhorse for versatile dimensional nanometrology tasks at the PTB [23].

Because of the increased sample height due to the introduction of the sphere rotation setup, we raised the z -position of the AFM head by introducing adapter rings in the metrology frame. Consequently, the AFM tip measures at a higher position than the so-called Abbe point, which is defined as the intersection point of the three measuring laser beams of x -, y - and z -interferometers, consequently introducing an Abbe-offset along the z -axis. Nevertheless, the AFM tip was still well aligned with the measurement beam of the z -interferometer. As the angle deviations around the x - and y -axes are controlled to be (almost) constant in NMM motions, the Abbe error of the whole measurement system can still be kept very small (a few nm or even below).

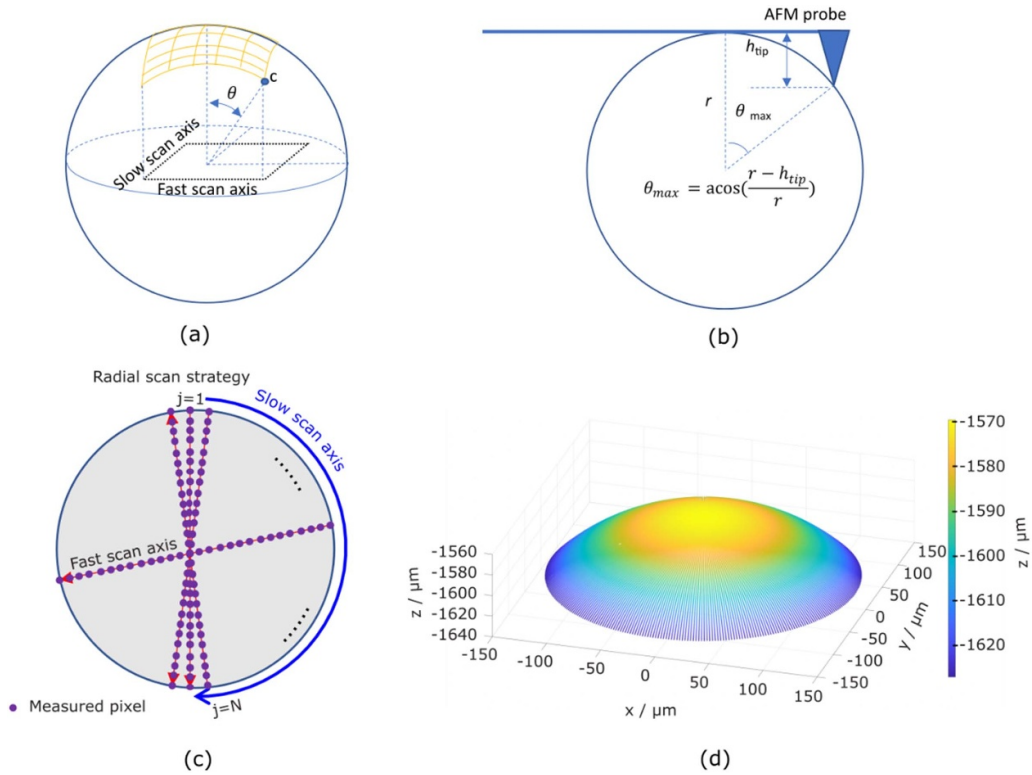


Figure 2. (a) Schematic diagram of conventional raster scan strategy; (b) maximal measuring spherical angle θ_{\max} measurable by an AFM tip with a tip height of h_{tip} ; (c) schematic diagram of the radial scan strategy; (d) an AFM image shown as raw data measured using the radial scan strategy at the sample orientation (γ, β) of $(0^\circ, 0^\circ)$.

2.2. Scan strategy

An AFM measurement is usually performed over a rectangular area in a Cartesian coordinate system, with its fast scan axis along one lateral axis and a slow axis along the other, as shown in figure 2(a). This scan strategy has however a disadvantage in measuring microspheres, namely that the spherical angle of the local surface under the AFM measurement (shown as θ in figure 2(a)) differs significantly at different scan lines. The corner positions of the measurement area (marked as c in figure 2(a)) correspond to a (much) higher spherical angle. It results in two problems: (a) a risk of mechanical collision between the sphere and AFM cantilever as illustrated in figure 2(b); and (b) the measurement accuracy is lower at a steeper surface, please refer to figure 7 of our previous publication [2].

To overcome these problems mentioned above, we applied a so-called radial scanning strategy for measuring the microsphere, as illustrated in figure 2(c). Using this scanning strategy, the apex of the microsphere was firstly determined, which can be conventionally achieved under the assistance of optical vision camera and several trial scans along the x - and y -axes. Then the fast scan profiles were arranged in radial direction through the apex, with the slow scan axis indicating the change of scan direction. The acquired pixels have equal distance along the radial direction and equal angular distance along the slow scan axis. It can be regarded as a ‘rectangular’ scan in the polar coordinate system. This scan strategy has

an advantage that the coverage of the spherical angle can be kept the same along different scan lines. However, it has also a disadvantage, namely that the pixels are not uniformly distributed. The pixel density is higher at areas closer to the apex. This issue can be solved by using a resampling processing in the data evaluation. In addition, possible measurement artefacts due to changed scan directions need to be further investigated as well.

An even better scan algorithm could have been a kind of fast spiral scanning strategy [24], which potentially offers a better coverage of spherical angle and a more uniform pixel distribution. However, it would need a more complicated motion control of the NMM, therefore, was not adopted in this study.

The maximal coverage of the spherical angle $(-\theta_{\max} \dots \theta_{\max})$ depends on the AFM tip height h_{tip} , and the radius of the microsphere being measured r . As shown in a simple schematic diagram in figure 2(b), one can easily get:

$$\theta_{\max} = \arccos\left(\frac{r - h_{\text{tip}}}{r}\right). \quad (1)$$

For achieving a large coverage of spherical angle in measurements, we applied an AFM probe with extra tall AFM tip (type SD-PXL-NCL from Nanosensor[®]) which has a nominal tip height of approximately $50 \mu\text{m}$. Thus, it has a theoretical $\theta_{\max} = 45.57^\circ$ for the sphere with $r = 200 \mu\text{m}$ measured in this study. In practice, we selected a scan range of $280 \mu\text{m}$

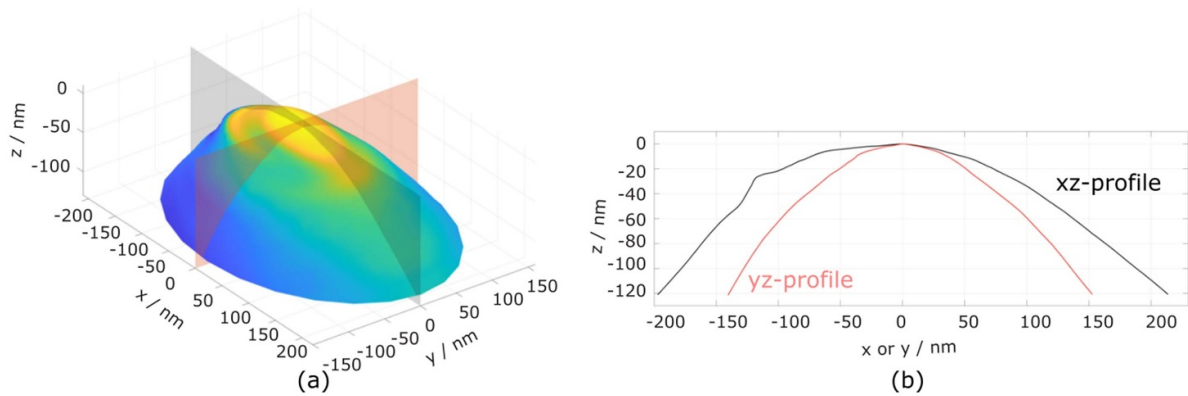


Figure 3. (a) 3D view of the characterised AFM tip shape; (b) cross-sectional profiles of the AFM tip via its tip-apex in the xz - and yz -planes, respectively.

along the fast radial scan direction, which corresponds to a coverage of spherical angle of $\pm 44.43^\circ$. It was slightly smaller than $\pm \theta_{\max}$. The reason is that we need to reserve an over-scanning length of approximately $2 \mu\text{m}$ along the fast scan axis. We acquired 180 scan lines per image and 14 001 pixels per fast scan line, which corresponds to a pixel distance of 20 nm along the fast scan axis and 1° along the slow scan axis. A representative AFM image measured using the applied scan strategy is shown in figure 2(d) as a raw measurement data set.

In this study, we measured the sphere at seven orientations with the combined roll and titling angles (γ, β) being $(0^\circ, 0^\circ)$, $(0^\circ, 60^\circ)$, $(60^\circ, 60^\circ)$, $(120^\circ, 60^\circ)$, $(180^\circ, 60^\circ)$, $(240^\circ, 60^\circ)$, $(300^\circ, 60^\circ)$, respectively. It is sufficient for covering the upper hemisphere with overlaps needed for stitching AFM images. To realise this measurement, the sphere needs to be rotated by R1 five times, while rotated by R2 only once. This is the reason why we implemented the R1 as a motorised stage while the R2 as a manual stage, which offers a good compromise between the measurement efficiency and the compactness of the mechanical set up. As the measurement chamber needs to be opened for rotating the sphere manually, an additional wait time (usually an overnight) for temperature stabilisation is required.

2.3. Characterisation of AFM tip geometry

AFM tip geometry is a key issue in AFM measurements. It directly impacts the tip-sample interaction force, which is the physical fundament of AFM measurements. The tip geometry defines the resolution capability of AFM measurements [25]. Measured AFM images are the dilated result of the real structure by the tip geometry [25], consequently it offsets the measurement results in the measurement of a microsphere. Therefore, in order to achieve traceable measurements of microspheres using the proposed method, the AFM tip geometry needs to be traceably characterised and then be applied to correct its contribution in measurements.

For characterising the tip geometry, a method developed in our previous study [26] was applied. The method uses a line width standard type IVPS100-PTB [27] as a tip

characterizer. The geometry of the line features has been accurately and traceably calibrated to the lattice constant of crystal silicon [28], which in turn offers the capability for traceable characterisation of AFM tip geometries. A measurement uncertainty down to approximately 1–2 nm of the developed method was reported in [26].

In this study, we characterised the tip applied for the measurements of microsphere in (almost) an identical way as in [2], where an accurately calibrated AFM tip was applied in calibrating the tip geometry of a stylus profilometer. For sake of brevity, we omit the details of the tip characterisation here. Readers are referred to [2, 26] for details concerning e.g. the measurement instrument, measurement procedures and data processing algorithms.

The characterised AFM tip geometry in this study is depicted in figure 3(a) as a 3D view. Two cross-sectional profiles through its tip apex in the xz and yz plane, respectively, are depicted in figure 3(b). They differ significantly, which is possible for a silicon tip due to the anisotropic behaviour of the crystal silicon.

We had only characterised the tip geometry after the measurements of the microsphere were finished. Consequently, we were not able to give quantitative information about the tip wear or tip breakage [29] during the AFM measurements of microsphere. As large range AFM measurements are prone to tip wear and tip breakage, e.g. which could come from accidental tip-sample touches, it would be important to check the scanning tip before and after and perhaps also during the measurements.

Some approaches can be taken to mitigate the problems of tip wear and tip breakage. For instance, it is a feasible approach to acquire AFM images after a tip is (slightly) worn by a few trial measurements. The tip wear is typically nonlinear, i.e. a sharp AFM tip is more prone to wear than a blunt one. Although a blunt tip leads to reduced lateral resolution, it is not a critical issue for the calibration of (micro)spheres in this study. In addition, AFM tips coated with better wear-resistant material such as diamond like carbon can be applied to reduce tip wear.

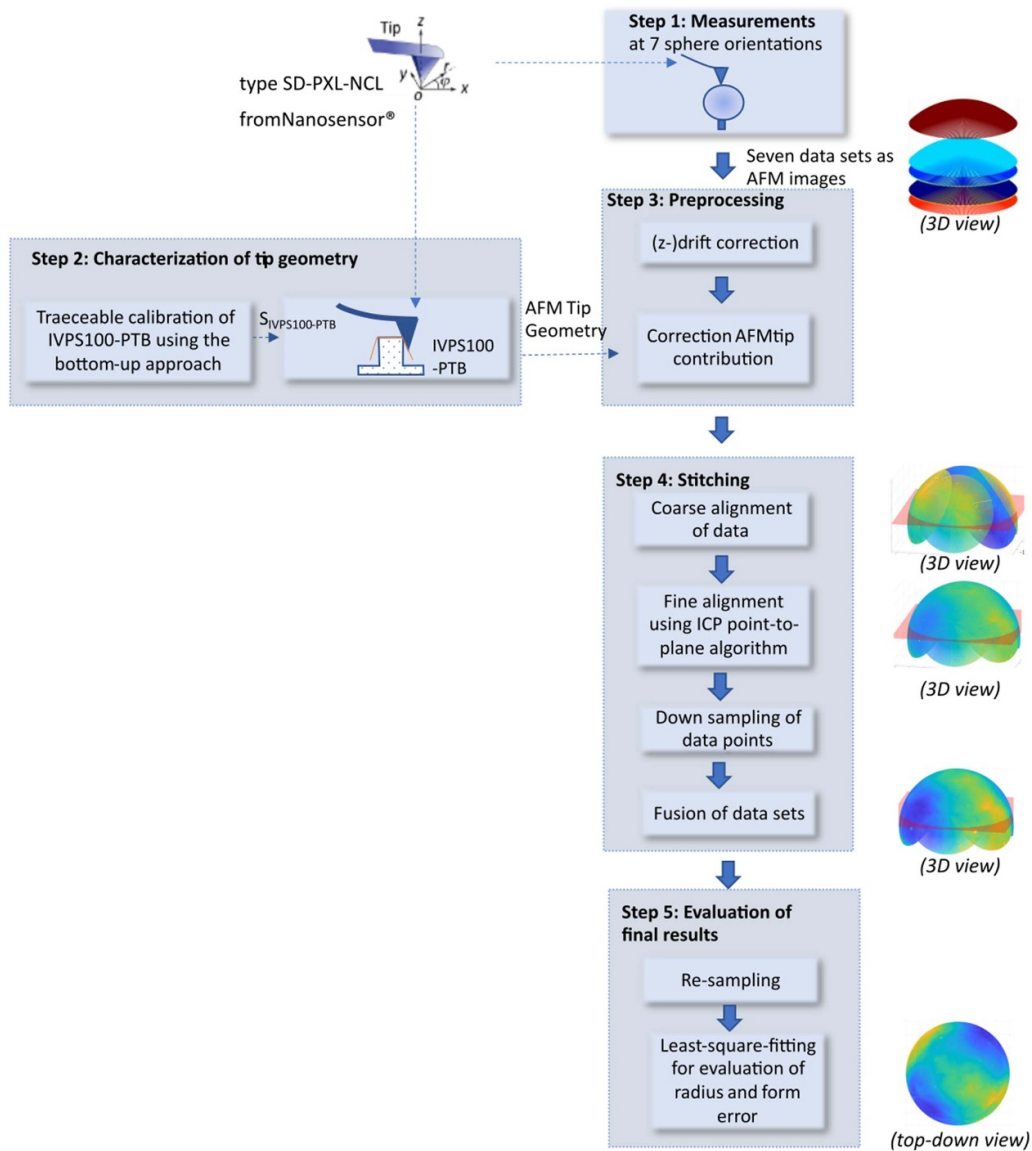


Figure 4. Schematic diagram of measurement and data evaluation procedures.

2.4. Measurement and data evaluation procedures

An overview of the measurement and data evaluation procedures is illustrated in figure 4. It consists of five steps. The first step was the measurement of the microsphere at seven orientations as detailed in §2.2. The second step was the characterisation of AFM tip geometry as mentioned in §2.3. The third step was the pre-processing of the AFM data sets. It aims to correct the known measurement distortions in the measured AFM images, such as the geometric errors, measurement drift and correction of tip contribution.

Geometric errors concern factors such as scaling factors, coupling factors and nonlinearities of AFMs. As the Met. LR-AFM applied in this study is a primary metrological tool, the correction of its geometric errors was not necessary. Nevertheless, if a normal AFM device is applied using the proposed method, such a correction would be necessary.

Measurement drifts refer to an uncontrolled relative motion of the tip and a sample, usually caused by thermal expansion [30]. As a scanning technique, AFM measurements are typically slow. Consequently, drifts will inevitably distort measured images, leading to measurement errors. For mitigating the impact of drifts, online and offline drift correction methods can be applied [30]. As the Met. LR-AFM is quite stable, in this study we have only applied a very simple algorithm for correcting the z -drift: as all radial scanning profiles cross the same apex point, the measured z -position of the apex point can be compared in sequential scan profiles for determining the z -drift. In practice, in order to reduce the influences such as measurement noise, surface roughness and lateral drifts, the averaged z -value of pixels which have distance to the apex point within $1 \mu\text{m}$ was applied for drift calculation. The observed drift reached up to 40 nm , and was around 20 nm for most measurements.

Correction of tip contribution can be performed using the morphological operation ‘erosion’ as detailed in [26]. In this study, we simply applied the software developed in [26] by inputting the measured raw AFM image and characterised tip geometry shown in figure 3. However, it should be mentioned that there was a little edge effect in applying the erosion method, which was introduced due to the unavailability of the pixels beyond the edge of AFM profiles when the tip geometry was eroded near the edge. To overcome this problem, 25 pixels from the edges of profiles were removed in the tip corrected profile.

The 4th step was the stitching of AFM data sets, and the final step was the evaluation and reporting of measurement results. They will be detailed in the next sections.

3. Stitching algorithms

Stitching of AFM data sets measured at different sample orientations is the most critical step in realising the proposed methodology. The performance of the data stitching will significantly impact the measurement uncertainty. As shown in figure 4, the stitching procedure consists of following tasks: coarse alignment, fine alignment, down-sampling, and fusion of data sets.

3.1. Coarse alignment

This task aims to coarsely align the data sets based on the combined roll and tilting angles (γ , β) of the sphere. The angles (γ , β) can be either the commanded/nominal value of the rotation stages (R1 and R2) or the angle readouts by sensors of the stages.

Each data set was firstly least square fit to a sphere. The coordinates of the centre of the fitted sphere, denoted as $O^i = (x_c^i, y_c^i, z_c^i)^T$ for the i th data set, were applied to shift the data sets all to the same origin of the global coordinate system. The coarse alignment can be written as:

$$\mathbf{p}_k^i = \mathbf{R}^i(\mathbf{m}_k^i - \mathbf{O}^i) \quad (2)$$

where, \mathbf{m}_k^i denotes the coordinates of k th point of the pre-processed i th data set, and \mathbf{p}_k^i denotes the coordinate of the point after coarse alignment. \mathbf{R}^i is the well-known 3D rotation matrix for the i th measurement:

$$\mathbf{R}^i = \mathbf{R}_y(\beta^i) \mathbf{R}_z(\gamma^i) = \begin{bmatrix} \cos\beta^i & 0 & \sin\beta^i \\ 0 & 1 & 0 \\ -\sin\beta^i & 0 & \cos\beta^i \end{bmatrix} \times \begin{bmatrix} \cos\gamma^i & -\sin\gamma^i & 0 \\ \sin\gamma^i & \cos\gamma^i & 0 \\ 0 & 0 & 1 \end{bmatrix} \quad (3)$$

where (γ^i, β^i) denotes roll and tilting angles (γ , β) of the sphere at the i th measurement.

Figure 5(a) illustrates the obtained data sets after coarse alignment, showing a good spheric form. However, deviations between data sets are clearly visible when they are coloured as

shown as a 3D view in figure 5(b) as well as a cross-sectional profile at the marked position in figure 5(c), which is arbitrarily selected and does not lie at an equator.

The coarse alignment procedure is capable of aligning individual segments with offsets in their overlapping areas mostly within 100 nm for the used datasets, offering a good initialization for the ICP fine alignment (detailed below), avoiding its convergence to a local minimum. The impact of the deviation of the coarse alignment on the fine alignment performance is expected to be below 0.5 nm.

3.2. Fine alignment

Fine alignment aims to reduce the deviations between data sets after coarse alignment. In this paper, we applied the ICP point-to-plane algorithm. As the algorithm was detailed in [31], its principle is only briefly introduced as shown in figure 6. For sake of simplicity, we consider two data sets denoted as \mathbf{P} and \mathbf{Q} . One of the data sets (\mathbf{Q}) is defined as fixed while the other (\mathbf{P}) is loose. For any point in data set \mathbf{P} , denote as \mathbf{p}_i , a point in data set \mathbf{Q} who has the smallest distance (i.e. the closest) to \mathbf{p}_i can be found, denoted as \mathbf{q}_i . The distance is simply calculated as the Euclidean distance in 3D space, denoted as $\|\mathbf{p}_i - \mathbf{q}_i\|$.

If the smallest distance $\|\mathbf{p}_i - \mathbf{q}_i\|$ is larger than a threshold value (3 μm in this study), \mathbf{p}_i was regarded as a non-overlap point between two data sets. Consequently, it was rejected from the calculation of fine alignment. Here the threshold value of 3 μm is a trade-off value selected experimentally. It should be larger than the possible largest $\|\mathbf{p}_i - \mathbf{q}_i\|$ in the overlapped region so that no valid data points in the overlapped region are wrongly rejected; while it should not be too large as otherwise it will introduce increased non-overlap points in fine alignment calculation which impacts its performance.

After the point \mathbf{q}_i was found, its normal vector \mathbf{n}_i was calculated. In a simplified illustration in figure 6(a), it was calculated by a least square plane fitting to its neighbouring points marked as $\mathbf{q}_i^a \sim \mathbf{q}_i^d$. However, in practice its neighbouring points within a predefined area size can be applied for fitting thus for reducing the influence of measurement noise. As the normal vectors for points in the fixed data sets \mathbf{Q} do not change in the whole iterative calculation process, the calculated values can be saved for following iterative calculations for enhancing calculation efficiency. The distance between the point \mathbf{p}_i and the local plane of \mathbf{q}_i can be calculated as $(\mathbf{p}_i - \mathbf{q}_i)^T \cdot \mathbf{n}_i$.

The task of the fine alignment is to rotate or translate the data set of \mathbf{P} (as a rigid body) so that the point-to-plane distance (of all selected points) is minimised. Mathematically, it can be written as the minimisation of the linearized objective function [31]:

$$E = \sum_i \left[(\mathbf{p}_i + \mathbf{r} \times \mathbf{p}_i + \mathbf{t} - \mathbf{q}_i)^T \cdot \mathbf{n}_i \right]^2 \quad (4)$$

where $\mathbf{r} = (\alpha_x, \alpha_y, \alpha_z)^T$ denotes a rotation vector with $\alpha_x, \alpha_y, \alpha_z$ being the angles about the x , y , and z -axes, respectively; $\mathbf{t} = (t_x, t_y, t_z)^T$ denotes a translation vector.

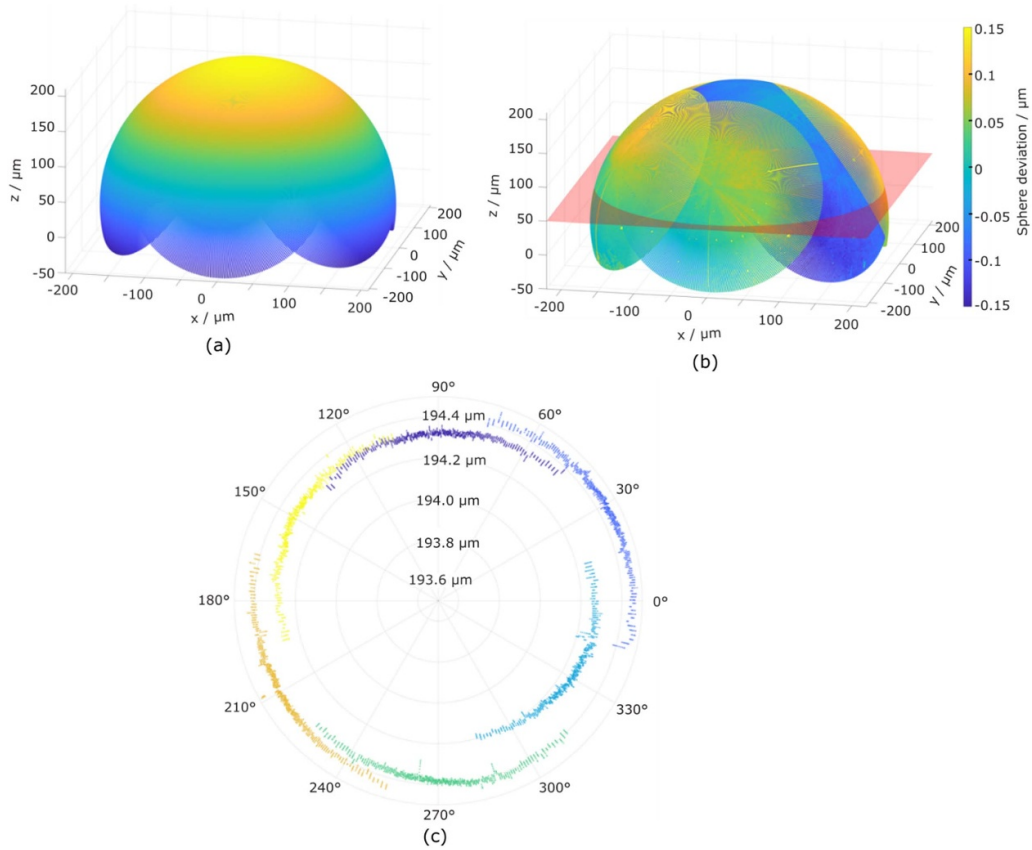


Figure 5. (a) Point cloud after merging the measured AFM data sets which are coarsely aligned according to the nominal orientations of samples in measurements; (b) merged data cloud with its sphere deviation coloured; (c) cross-sectional profile of the merged data cloud at the marked plane in (b).

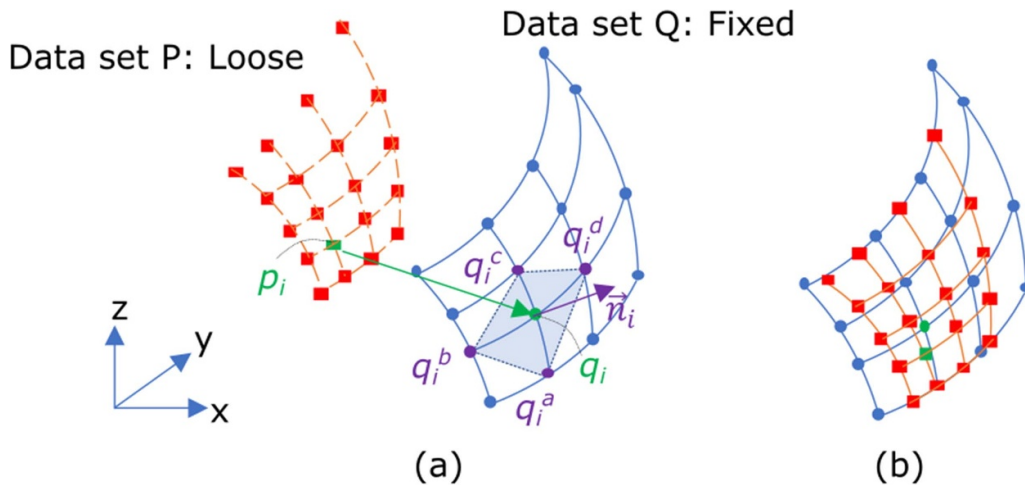


Figure 6. Schematic diagram showing the principle of the iterative closest point (ICP) point-to-plane algorithm for matching of two surface data sets, shown (a) before and (b) after objective function minimizing transformation.

However, in this study we only calculated the translation vector t while keeping the rotation vector r as $\mathbf{0}$ due to two important reasons. The first reason is due to the fact that the sphere we measured has very good sphericity as indicated in figure 7, i.e. rotation symmetry. Consequently, the objective function is very insensitive to the rotation vector r , leading to an illness problem in minimising the objective

function. In [16], the rotation of profile segments was fine aligned eventually based on the matching of (local) roundness deviations in different segments. However, as they only measured a great circle of a sphere, the complexity of the measurement and of the fine alignment calculation is (much) smaller than in our study. Theoretically speaking, we can also apply the (local) form error of the sphere for fine rotational

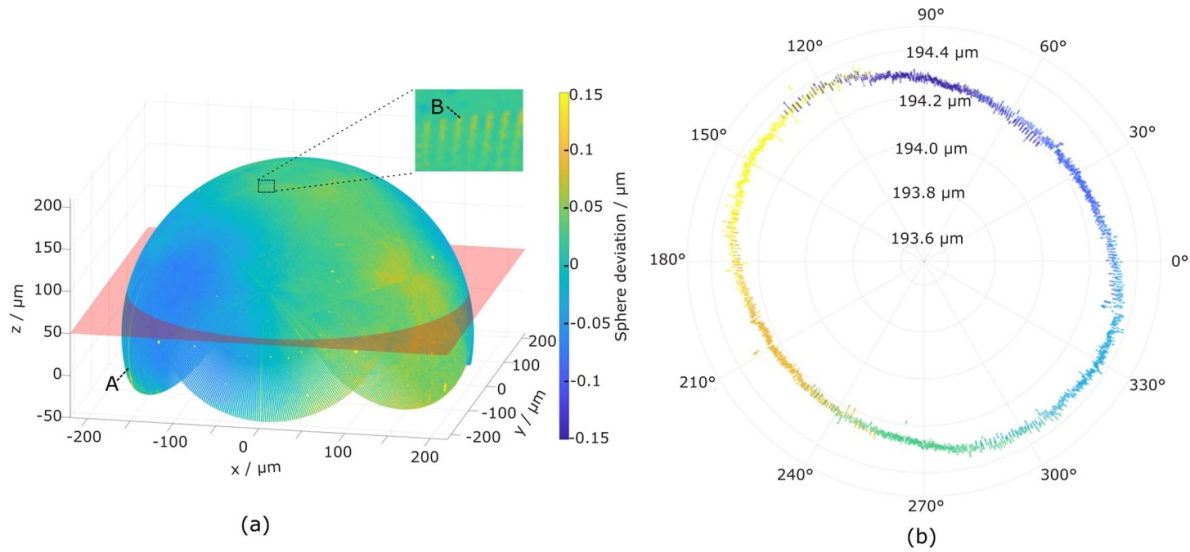


Figure 7. (a) Fine aligned point clouds after the ICP point-to-plane algorithm with the colour indicating the sphere deviation; (b) cross-sectional profile of the fine aligned point clouds at the marked plane in (a).

alignment of the data sets, however, it needs the sphere surface to be measured with a higher pixel density, which would in turn lead to practical problems such as increased measurement time, larger measurement drift, stronger tip wear and longer data processing time. Another important reason is due to the fact that unlike the translation vector t , the rotation vector r is quite insensitive to the measurement uncertainty of size and form error of the sphere, consequently the angular accuracies of the rotation stages are sufficient. Therefore, the omittance of fine alignment rotational angles is an acceptable compromise among measurement efforts, complexity of data evaluation and measurement uncertainty. In this study, ICP algorithm has been tried with fine alignment of rotational angles enabled, however, it did not result in an improved performance.

The translation vector t can be easily solved using the linear algebra method. After moving the data set \mathbf{P} by t , the alignment between \mathbf{P} and \mathbf{Q} can be improved, as illustrated in figure 6(b). By iteratively executing the alignment procedures mentioned above, a fine alignment with desired quality can be achieved.

The ICP point-to-plane fine alignment mentioned above can be performed either in a pairwise way or simultaneously for all data sets. In this study we performed alignment simultaneously for all data sets. After 20 iterations, we obtained satisfying alignment results as shown in figure 7, which shows the 3D data sets with coloured sphere deviations (a) and a cross-sectional profile in (b). Compared to the coarsely aligned data sets shown in figure 5, the alignment between data sets was clearly improved. In this study, a fixed iteration number of 20 is set as the stopping criteria of the ICP algorithm, what provided well converged alignment results. Currently, the calculation takes approximately 75 min using a desktop PC; however, this can be optimized.

Interestingly, having a close look at the fine aligned data we can find several ‘mismatching’ artefacts, which can be attributed to AFM measurement effects. For instance, the artefact marked as ‘A’ in figure 7(a) can be attributed to a profile

‘jump’ effect, which was typically caused by the pick-up of a contamination particle by the AFM tip during measurements. In the inset of figure 7(a), some slight mismatching of data sets can be observed marked as ‘B’. It typically happened at the edge region of data sets, due to the fact that the measurement accuracy of (conventional) AFM profiles is typically lower in the measurements of surface with larger tilting angles.

3.3. Down sampling and data fusion

After the ICP point to plane fine alignment, the different data sets are merged (i.e. fused) into one data set. However, as each (pre-processed) data set contains a large number of pixels (i.e. 13951×180 pixels), it takes lots of computation power. To mitigate this problem, the data sets were down sampled before data fusion. The sphere was divided into many cubic voxels with a side length of $0.5 \mu\text{m}$. For each voxel only the pixel which was closest to the centre of the voxel was kept while other pixels were removed, decreasing the calculation time and number of pixels by a factor of around 20 and increasing data homogeneity.

The data fusion was performed by averaging the down sampled pixels, which led to a smoother surface. For the averaging, the sphere centre of the down sampled pixels was first calculated by least square fitting. Then, for each pixel its neighbouring pixels who have a distance, r_{avg} , less than a given value ($3 \mu\text{m}$ and $8 \mu\text{m}$ in this study, results compared in table 1) to the pixel were collected. The radii of the pixel and neighbouring pixels were then averaged to calculate the fused result of the pixel. The fused result is shown in figure 8(a) as a 3D view and figure 8(b) as a cross-sectional profile at the marked position. A same inset figure as in figure 7(a) is also plotted in figure 8(a). The artefact marked at ‘B’ in figure 7(a) is no more visible in figure 8(a) owing to the averaging effect.

Table 1. Evaluated radius of the measured microsphere. All data are given in μm .

| Measurements | $l_{rs} = 0.0 \mu\text{m}$ | | $l_{rs} = 0.5 \mu\text{m}$ | $l_{rs} = 2 \mu\text{m}$ |
|------------------------|----------------------------------|----------------------------------|----------------------------------|--------------------------|
| | $r_{\text{avg}} = 8 \mu\text{m}$ | $r_{\text{avg}} = 3 \mu\text{m}$ | $r_{\text{avg}} = 8 \mu\text{m}$ | |
| Tip corrected, Run 1 | 200.648 | 200.649 | 200.648 | 200.653 |
| Tip corrected, Run 2 | 200.655 | 200.656 | 200.656 | 200.661 |
| Tip corrected, Run 3 | 200.659 | 200.661 | 200.660 | 200.665 |
| Tip corrected, Run 4 | 200.654 | 200.655 | 200.655 | 200.660 |
| Mean | 200.654 | 200.655 | 200.655 | 200.660 |
| Standard deviation | 0.005 | 0.005 | 0.005 | 0.005 |
| Tip uncorrected, Run 1 | 200.788 | 200.789 | 200.789 | 200.796 |
| Tip uncorrected, Run 2 | 200.798 | 200.799 | 200.799 | 200.805 |
| Tip uncorrected, Run 3 | 200.803 | 200.804 | 200.804 | 200.811 |
| Tip uncorrected, Run 4 | 200.798 | 200.799 | 200.799 | 200.806 |
| Mean | 200.797 | 200.798 | 200.798 | 200.804 |
| Standard deviation | 0.006 | 0.007 | 0.007 | 0.006 |

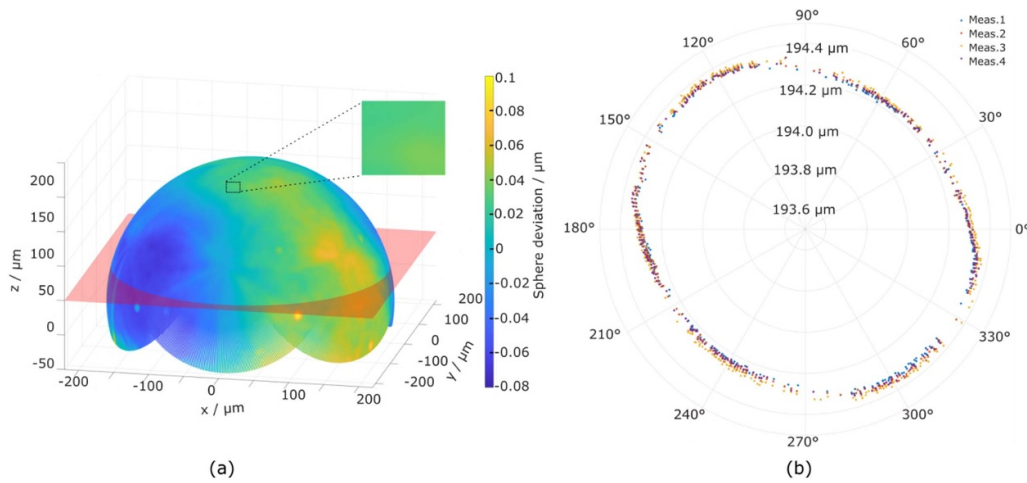


Figure 8. (a) Fused point cloud with the colour indicating the sphere deviation; (b) cross-sectional profile of the fused point cloud at the marked plane in (a) of four repeated measurements.

It should be mentioned that the data points in figure 8(b) look unevenly distributed. However, it is an effect of data illustration only. If we select a ‘thicker’ cross-sectional plane, the distribution of pixels will appear much more evenly distributed. We have plotted the cross-sectional profiles in figures 5(c), 7(b) and 8(b) at the same z position and with the same thickness so that the change of the data points after different data processing steps can be clearly visible.

In this study, the whole stitching process was executed in a Matlab® program using a desktop PC with an Intel core i9-9900 CPU and 64 GB RAM, which takes approximately three hours. Nevertheless, there is much room available for improving the algorithm, thus for reducing the computation time.

4. Result

As the radial scanning strategy delivers data points which are not evenly distributed on the spheric surface and as pixel numbers are larger in the overlapping areas of the datasets, it is an option to re-sample the fused data set for obtaining evenly

distributed data points. This re-sampling after the fusion has been done using again rectangular voxels with a side length l_{rs} of $0 \mu\text{m}$, $0.5 \mu\text{m}$ and $2 \mu\text{m}$ (results compared in table 1), where $l_{rs} = 0 \mu\text{m}$ indicates no re-sampling applied. The evaluation of the size and form error of the measured sphere afterwards is rather straight forward, by simply least square fitting the fused data set to a sphere.

To illustrate the measurement stability of the developed method, we performed four sets of repeated measurements. The finally evaluated form errors of four repeated measurements are depicted in figures 9(a)–(d), respectively. It can be clearly seen that the results agree well with each other, indicating the stability and robustness of the developed method. Some slight discrepancies are visible, e.g. an artefact marked as A in figure 9(d) is not visible at the same position in figure 9(c). Such artefact can be attributed to the profile ‘jump’ effects in AFM measurements. They can be further eliminated by marking them as outliers and thus being removed from data sets.

The evaluated results of sphere radius are summarised in table 1. To investigate the influence of tip geometry and the selection of evaluation parameters on the results, the evaluation was performed in different conditions:

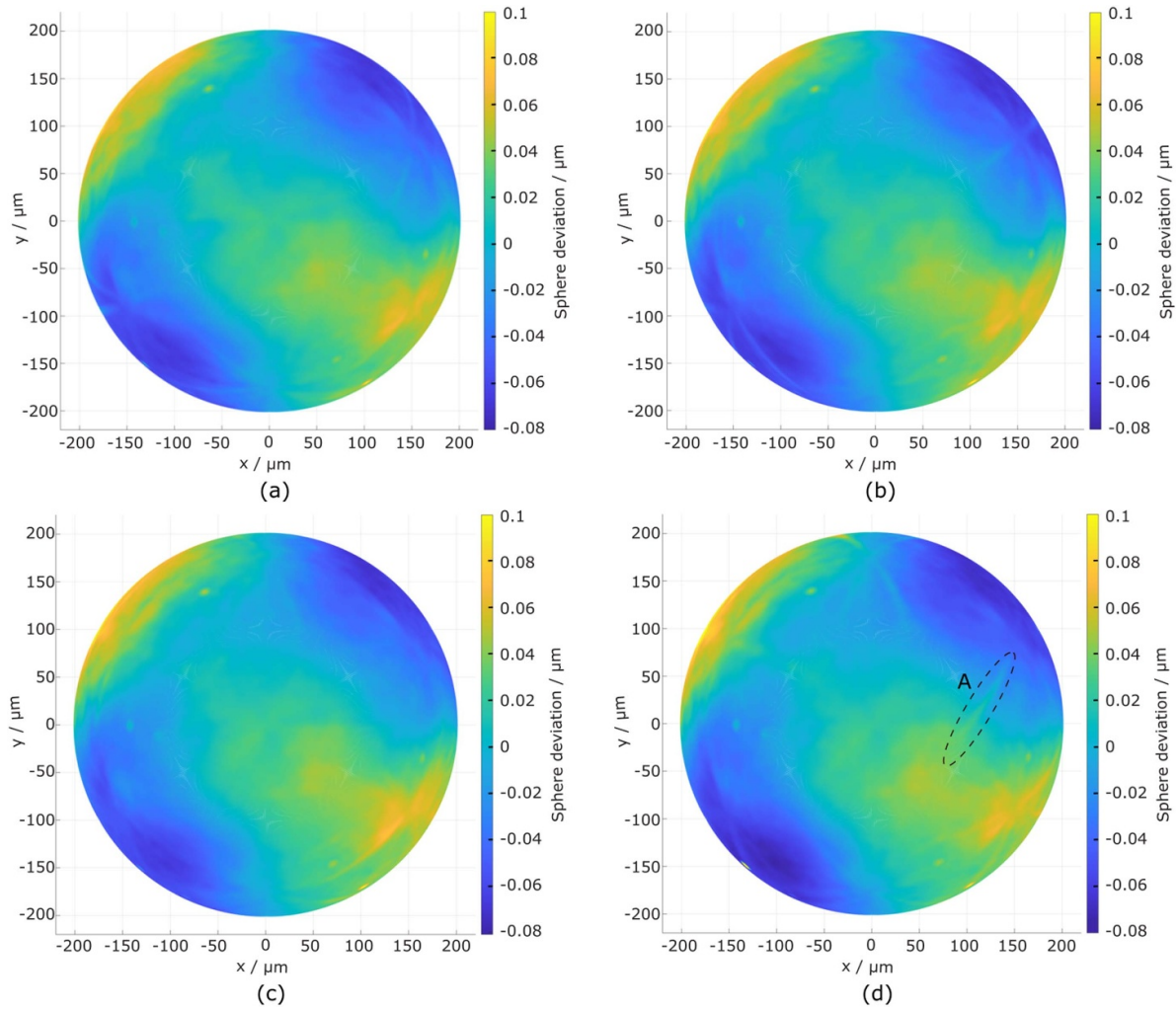


Figure 9. Form error of the sphere measured in four repeated measurements shown as (a)–(d).

- (a) With and without the correction of the AFM tip geometry.
 (b) With different averaging sizes of data fusion r_{avg} selected as 8 μm and 3 μm without re-sampling i.e. with $l_{\text{rs}} = 0.0 \mu\text{m}$.
 (c) With different size of resampling l_{rs} selected as 0.5 μm and 2 μm under the same $r_{\text{avg}} = 8.0 \mu\text{m}$.

The results clearly show that the selected evaluation parameters l_{rs} and r_{avg} have little influence on the evaluated radius values. However, the difference between the radius values evaluated with and without tip correction reaches approximately 140 nm, indicating the importance the AFM tip correction. The standard deviation of evaluated radii of four repeated measurements reaches 5 nm for the tip corrected results, indicating high stability and robustness of the developed method.

5. Conclusion

Spheres are widely applied in dimensional metrology either as probing spheres of tactile tools such as CMMs or in physical standards for the embodiment of dimensions. Accurate

and traceable metrology of the size and form error of these spheres, particularly for small spheres, remains as a challenge today.

This paper presents a method for accurate measurements of size and form of a microsphere by acquiring a set of seven AFM images at different orientations of the spheres. The set of AFM images are finely aligned with each other using the ICP point-to-plane algorithm. They are then fused to one data set, from which the size and form can be evaluated.

Using this method, the AFM tip geometry is an important influencing factor as the measured AFM image is the dilated result of the measured structure by its tip geometry. To realise traceable calibration of the microsphere, the AFM tip geometry needs to be traceably calibrated, too. To solve this problem, the AFM tip geometry was traceably calibrated to a line width standard type IVPS100-PTB, whose feature geometry was calibrated with a traceable route to the lattice constant of crystal silicon.

Measurement setup, scan strategy, and data evaluation processes have been detailed in the paper. Evaluated size and form error of the microsphere in four repeated measurements are reported, showing promising measurement performance.

For instance, the standard deviation of measured radius values from four repeated measurements reaches 5 nm.

However, many research works need to be done further to make the method merit for calibration service, for instance:

- (a) To characterise the AFM tip geometry before and after measurements of microspheres thus to investigate the tip wear and its impacts on measurements.
- (b) To develop drift correction method along x , y , and z -axis. Drift leads to distortion of AFM images, thus impacting the measurement performance.
- (c) To further improve the algorithm to reduce the data processing time.
- (d) To perform reproducible measurements by using e.g. different AFM tips, different scanning speeds and scanning directions, and to conduct comparisons with peer-researchers to verify the metrology performance.
- (e) To set up the measurement uncertainty budget of the develop method.

The ultimate research goal is to achieve the so-called bottom-up approach for traceable and accurate metrology of micro and nanostructures [28, 32, 33].

Data availability statement

The data generated and/or analysed during the current study are not publicly available for legal/ethical reasons but are available from the corresponding author on reasonable request.

Acknowledgments

This project has received funding from the EMPIR programme co-financed by the Participating States and from the European Union's Horizon 2020 research and innovation programme with the Grant Number of '20IND08 MetExSPM'.

Statement

The paper has no conflict of interest. The contributions of authors are as follow: G D proposed the measurement methodology, organised the whole research and wrote the paper. J D performed the data processing and data evaluation. X H executed the measurements. H W prepared the mechanical setup. R T supervised the PhD thesis of J D and discussed the results. E M stimulated the research idea and discussed the results. All authors proof-read the paper.

ORCID iDs

Gaoliang Dai  <https://orcid.org/0000-0002-1611-0074>

Johannes Degenhardt  <https://orcid.org/0000-0001-5508-5556>

Xiukun Hu  <https://orcid.org/0000-0003-1780-5801>

Eberhard Manske  <https://orcid.org/0000-0002-1672-2978>

References

- [1] Weckenmann A, Estler T, Peggs G and McMurtry D 2004 Probing systems in dimensional metrology *CIRP Ann.* **53** 657–84
- [2] Dai G, Hu X and Degenhardt J 2022 Bottom-up approach for traceable calibration of tip geometry of stylus profilometer *Surf. Topogr.: Metrol. Prop.* **10** 015018
- [3] Becker P, Bettin H, Danzebrink H-U, Gläser M, Kuetgens U, Nicolaus A, Schiel D, De Bièvre P, Valkiers S and Taylor P 2003 Determination of the Avogadro constant via the silicon route *Metrologia* **40** 271–87
- [4] Carmignato S, Chiffre L D, Bosse H, Leach R K, Balsamo A and Estler W T 2020 Dimensional artefacts to achieve metrological traceability in advanced manufacturing *CIRP Ann.* **69** 693–716
- [5] Bartl G, Bettin H, Krystek M, Mai T, Nicolaus A and Peter A 2011 Volume determination of the Avogadro spheres of highly enriched ^{28}Si with a spherical Fizeau interferometer *Metrologia* **48** 96–103
- [6] Dai G, Neugebauer M, Stein M, Bütefisch S and Neuschaefer-Rube U 2016 Overview of 3D micro- and nanocoordinate metrology at PTB *Appl. Sci.* **6** 257
- [7] Yu H, Huang Q and Zhao J 2014 Fabrication of an optical fiber micro-sphere with a diameter of several tens of micrometers *Materials* **7** 4878–95
- [8] Thalmann R, Meli F and Küng A 2016 State of the art of tactile micro coordinate metrology *Appl. Sci.* **6** 150
- [9] Küng A and Meli F 2005 Self calibration method for 3D roundness of spheres using an ultraprecision coordinate measuring machine *Proc. 5th Euspen Int. Conf. (Montpellier, France, May 2005)* vol 1 p 193
- [10] Neugebauer M 2011 EURAMET Project 1105, Bilateral comparison on micro-CMM artefacts between PTB and METAS, Final report
- [11] Kondo Y, Hirai A and Youichi B 2022 Two-point diameter calibration of a sphere using a micro-coordinate measuring machine at NMIJ *Metrologia* **59** 024005
- [12] Michihata M, Hayashi T, Adachi A and Takaya Y 2014 Measurement of probe-stylus sphere diameter for micro-CMM based on spectral fingerprint of whispering gallery modes *CIRP Ann.* **63** 469–72
- [13] Medicus K M and Jansen M 2010 Diameter measurement of small spheres on a white light interferometer including uncertainty analysis *Proc. Euspen Int. Conf. Delft, Netherlands* vol 1 p 75
- [14] Schaude J, Baumgärtner B and Hausotte T 2021 Bidirectional confocal measurement of a microsphere *Appl. Opt.* **60** 8890–5
- [15] Fan K, Wang N, Wang Z-W and Zhang H 2014 Development of a roundness measuring system for microspheres *Meas. Sci. Technol.* **25** 064009
- [16] Oertel E and Manske E 2021 Radius and roundness measurement of microspheres based on a set of AFM surface scans *Meas. Sci. Technol.* **32** 044005
- [17] Oertel E and Manske E 2022 Influence of form deviations on the radius and roundness measurement of microspheres *TM Tech. Mess.* **89** 704–13
- [18] Zhao X S, Sun T, Yan Y D, Li Z Q and Dong S 2006 Measurement of roundness and sphericity of the microsphere based on atomic force microscope *Key Eng. Mater.* **315-316** 796–9
- [19] Dai G, Pohlenz F, Danzebrink H-U, Xu M, Hasche K and Wilkening G 2004 Metrological large range scanning probe microscope *Rev. Sci. Instrum.* **75** 962
- [20] Manske E, Hausotte T and Jäger G 2007 New applications of the nanopositioning and nanomeasuring machine by using advanced tactile and non-tactile probes *Meas. Sci. Technol.* **18** 520

- [21] Dai G, Wolff H, Pohlenz F and Danzebrink H-U 2009 A metrological large range atomic force microscope with improved performance *Rev. Sci. Instrum.* **80** 043702
- [22] Dai G, Zhu F and Fluegge J 2015 High-speed metrological large range AFM *Meas. Sci. Technol.* **26** 095402
- [23] Dai G and Hu X 2022 Correction of interferometric high-order nonlinearity error in metrological atomic force microscopy *Nanomanuf. Metrol.* **5** 412–22
- [24] Mahmood I A and Reza Moheimani S O 2009 Fast spiral-scan atomic force microscopy *Nanotechnology* **20** 365503
- [25] Dixon R, Orji N, Misumi I and Dai G 2018 Spatial dimensions in atomic force microscopy: instruments, effects, and measurements *Ultramicroscopy* **194** 199–214
- [26] Dai G, Xu L and Hahm K 2020 Accurate tip characterization in critical dimension atomic force microscopy *Meas. Sci. Technol.* **31** 074011
- [27] Dai G, Zhu F, Heidelmann M, Fritz G, Bayer T, Kalt S and Fluegge J 2015 Development and characterisation of a new line width reference material *Meas. Sci. Technol.* **26** 115006
- [28] Dai G, Heidelmann M, Kübel C, Prang R, Fluegge J and Bosse H 2013 Reference nano-dimensional metrology by scanning transmission electron microscopy *Meas. Sci. Technol.* **24** 085001
- [29] Strahlendorff T, Dai G, Bergmann D and Tutsch R 2019 Tip wear and tip breakage in high-speed atomic force microscopes *Ultramicroscopy* **201** 28–37
- [30] Degenhardt J et al 2021 Flexible correction of 3D non-linear drift in SPM measurements by data fusion *Meas. Sci. Technol.* **32** 035005
- [31] Glira P, Pfeifer N, Briese C and Ressler C 2015 A correspondence framework for ALS strip adjustments based on variants of the ICP algorithm *Photogramm. Fernerkun. Geoinf.* **2015** 275–89
- [32] Oertel E and Manske E 2022 Ein bottom-up ansatz für die radius- und rundheitsmessung von mikrokugeln *TM Tech. Mess.* **89** 101–6
- [33] Dai G, Koenders L, Fluegge J and Bosse H 2016 Two approaches for realizing traceability in nanoscale dimensional metrology *Opt. Eng.* **55** 091407